International Journal of Heat and Mass Transfer 229 (2024) 125660

Contents lists available at ScienceDirect

International Journal of Heat and Mass Transfer

journal homepage: www.elsevier.com/locate/hmt

Design of heat pipes on board accelerating vehicles using the 1D/3D co-simulation approach

Matteo Ermini [a,*], Massimo Sabato [a], Federico Brusiani [b], Thierry Baritaud [b], Roberto Corsini [a], Enrico Stalio [a]

[a] Dipartimento di Ingegneria Enzo Ferrari, Università di Modena e Reggio Emilia, via Pietro Vivarelli 10, 41125 Modena, Italy
[b] Ferrari S.p.A., via Enzo Ferrari, 27, 41053 Maranello, Italy

ARTICLE INFO

Keywords:
Heat pipe
LPTN
1D/3D co-simulation
OpenFOAM
Power electronics

ABSTRACT

When a heat pipe is used as a cooling system for road vehicles, it is subject to acceleration which can adversely affect its thermal performance. In this study, we investigate the possibility of applying heat pipes for the cooling of power modules subject to time-varying power dissipation and time-dependent acceleration vectors whose projection along the heat pipe axis is up to $3g$. The problem is tackled by modelling the heat pipe through a lumped parameter thermal network (LPTN). A numerical algorithm is used to solve the equations of LPTN representing the heat pipe. The code is then coupled with a $3D$ CFD solver (*OpenFOAM*) to perform a 1D/3D co-simulation and test the applicability of heat pipes as the cooling system in high-performance cars.

1. Introduction

The design of cooling systems for power modules involves the transport of heat at high power density. A heat pipe is a passive cooling device that transports heat from a heat source to a sink *via* phase change. In some applications, this results in a highly efficient, heat transfer system [1,2]. Besides power modules (see for example [3]), heat pipes are also applied to other electronic devices [4].

The behaviour of heat pipes has been investigated following different approaches. Experimental studies provide useful information about heat pipe operation and performance. For example, Huang et al. [5] and El-Genk et al. [6] investigate the transient response of a heat pipe measuring the wall and vapour temperature when the evaporator is subject to step changes in input power. Garimella et al. [7] characterises the performance of the heat pipe wick by measuring the mass flow rate of the working fluid and its temperatures. Wang et al. [8] study the pressure difference between the condensing and boiling sections in a heat pipe.

Scott and Kirk [9] perform experiments on a flexible heat pipe subject to a transient radial acceleration; Kiseev et al. [10] and Zaghdoudi & Sarno [11] show the effect of accelerations on a flat plate heat pipe.

In parallel with the experimental works, researchers have developed analytical models of different complexity. Riffat et al. [12] investigates the performance of mini and micro heat pipes where gravitational effects are included. Zhu & Vafai [13] have developed a two-dimensional analytical model for the steady-state operation of cylindrical heat pipes which incorporates the liquid–vapour interfacial forces and also the non-Darcian (quadratic) term in the wick. Also, the case of heat pipes inclined with respect to gravity can be tackled analytically [14].

The numerical approach can be two- or three-dimensional or use a lumped parameter model. Tournier et al. [15] have developed a two-dimensional Finite Volume model to simulate the transient behaviour of a heat pipe, the model is validated against experimental data from Huang et al. [5]. Sun et al. [16] investigated the three-dimensional, steady-state behaviour of a set of heat pipes, including the single heat pipe failure and the heat pipes cascade failure accident. The three-dimensional, unsteady operation of a heat pipe has been represented numerically by Höhne [17] to assess its behaviour and thermal performances. A convenient numerical representation of a heat pipe is through a transient thermal network. The first unsteady model in the literature is described by Zuo & Faghri [18]. The model is compared with the experimental data by El-Genk [6], and its behaviour in time is found to be slightly faster than the measured one. Ferrandi et al. [19] have developed a lumped parameter numerical model to simulate the transient operation of sintered heat pipes. The code is validated in unsteady conditions by comparison with experimental results [5] and numerical results [15]. In the steady state case, the code is also validated against analytical results [13]. Caruana et al. [20] developed a lumped parameter model to simulate the transient operation of a heat pipe including gravity and real gas effects which are not included

* Corresponding author.
E-mail address: matteo.ermini@unimore.it (M. Ermini).

https://doi.org/10.1016/j.ijheatmasstransfer.2024.125660
Received 19 January 2024; Received in revised form 29 April 2024; Accepted 1 May 2024
Available online 16 May 2024

by [19]. The focus of Ref. [20] is on the error brought by the representation of the vapour phase by the ideal gas law. In the present study, a time-dependent volumetric source of momentum is added to the lumped parameter formulation in Ref. [19]. The additional term can represent accelerations with respect to an inertial frame of reference. In addition and in view of practical applications, lumped parameter models can be conveniently coupled to three-dimensional, unsteady simulations in order to fully represent the complex interaction between heat sinks and systems in the effort to achieve thermal control.

The 1D/3D co-simulation approach, see for example Refs. [21–24], is conveniently used when the system of interest is too complex and computationally expensive for a full three-dimensional unsteady CFD simulation, while a one-dimensional network representation might be inaccurate in the regions where fluid flow and heat transfer are highly three-dimensional. It allows to treat by a lumped parameter model (1D) selected components of the investigated system, which are easier to model than to fully represent by using CFD. This is the case of a pipe network, easily amenable to a lumped parameter model or a heat pipe where evaporation, condensation and capillarity effects are accounted for through simple lumped parameter models. In this case, it can be convenient to resort to 1D/3D co-simulation where the time-dependent lumped parameter approach is coupled to three-dimensional unsteady thermal and fluid mechanics simulations.

This work is motivated by the possible application of cooling systems based on passive loops on accelerating road vehicles, where the projection of the acceleration vector along the heat pipe axis is of order a few times g. An unsteady volumetric source of momentum is added to the lumped parameter representation of heat pipes found in the literature [19]. Tests are carried out in a practical high-performance car application. The present work clarifies how the effect of strong accelerations can be successfully implemented in a lumped parameter heat pipe model.

On the one side, we investigate the possibility of applying heat pipes to the cooling of accelerating mechanical systems. In addition, we implement the 1D/3D co-simulation approach to test its applicability and convenience. For the particular case under scrutiny, it is found that when the accuracy required in the prediction of the temperature level of critical regions of the system is high, the effect of accelerations of order a few times g should be accounted for.

2. Numerical method

The problem of modelling a heat pipe is tackled here by an unsteady lumped parameter approach. Accordingly, a fluid network is introduced coupled to a thermal network, the two networks are defined in the same region.

2.1. A coupled two-phase fluid and thermal model for heat pipe representation

In the context of this approach, the physical domain is subdivided into Control Volumes (CVs). One single, jth value for each unknown is associated with the jth Control Volume, these values should be interpreted as space-averaged values. Fluxes of mass, momentum and energy are calculated between CVs.

The numerical reduces to the solution of a number of algebraic equations, which corresponds to the product of the number of unknown fields times the number of control volumes representing the system in consideration. Such algebraic equations descend from their differential counterparts through discretisation. Differential equations enforce mass conservation, momentum balance and thermal energy balance. The heat pipe system is subdivided into $n_{\mathrm{cv}} = 8$ CVs, as displayed in Fig. 1. Tables 1 and 2 report the list of unknowns, together with the indication of the equation associated with the specific unknown. Not all of the CVs are associated with an equal number of unknowns: velocity and pressure are not defined in CVs in solid regions. Pressure and temperature in the vapour phase of the evaporator and the condenser are almost equal because of the very small losses encountered by the fluid flow in the heat pipe core and the circumstance that the process there is isothermal. As a consequence, only two control volumes are defined in the vapour region, see again Fig. 1. The 17 unknowns introduced in Tables 1 and 2 correspond to an equal number of equations, see the semi-discrete equations, (2.1) to (2.17).

Equations from (2.13) to (2.16) represent the spatially discrete mass conservation equations in the corresponding CV, enforced at the porous material close to the evaporator and condenser and at the clear vapour region of the evaporator and condenser. Eqs. (2.11) to (2.12) represent the axial projection of the spatially discrete momentum equations in the vapour region, Eq. (2.11), and in the liquid-saturated porous material, Eq. (2.12). The additional term (ρa_z) represents the zth projection (where z is the heat pipe axial direction) of fictitious forces per unit volume due to a possibly non-inertial frame of reference. The Young–Laplace equation (2.17) enforces the relation between pressure drop across a curved liquid–vapour interface and surface tension.

Equations from (2.1) to (2.6) represent the semi-discrete heat conduction equations, Eq. (2.1) includes also a source of energy, which represents heat subtracted from the device to be cooled. With reference to Fig. 1 the six equations represent thermal balances of the solid wall region at the evaporator, solid wall region at the condenser, porous material at the evaporator, porous material at the condenser, the solid wall of the adiabatic region and finally, the porous material at the adiabatic region. Eqs. (2.7) and (2.8) represent the progress in time of adiabatic transformations of an ideal gas. There, the assumption that thermodynamic formulas derived for equilibrium systems may be applied locally in non-equilibrium contexts, is considered valid. Eqs. (2.9) and (2.10) are obtained from the definitions of latent heat of vaporisation λ_α and condensation λ_β together with the definitions of thermal resistances R between CVs: R_{ep-ev} and R_{cp-cv}, see Fig. 1. When two letters are given in the subscript, the first makes reference to the control volume (a - adiabatic, c - condenser, e - evaporator) the second to the sub-component (p - porous, w - wall) or to the phase of the fluid (ℓ - liquid, v - vapour), depending if it is under scrutiny the solid material or the fluid phase. The nomenclature is also with reference to the schematics of the heat pipe given in Fig. 1. The subscripts of thermal resistances instead refer to the two control volumes sharing the heat flux, subject to the resistance.

Thermal equations:

$$
\begin{cases}
C_{ew}\dfrac{dT_{ew}}{dt} = \dot{Q}_{in} - \dfrac{T_{ew}-T_{aw}}{R_{aw-ew}} - \dfrac{T_{ew}-T_{ep}}{R_{ep-ew}} & (2.1)\\
C_{ep}\dfrac{dT_{ep}}{dt} = \dfrac{T_{ew}-T_{ep}}{R_{ep-ew}} - \dfrac{T_{ep}-T_{ap}}{R_{ap-ep}} - \dfrac{T_{ep}-T_{ev}}{R_{ep-ev}} & (2.2)\\
C_{cw}\dfrac{dT_{cw}}{dt} = \dfrac{T_{aw}-T_{cw}}{R_{aw-cw}} - \dfrac{T_{cp}-T_{cw}}{R_{cp-cw}} - \dfrac{T_{cw}-T_{f}}{R_{f-cw}} & (2.3)\\
C_{cp}\dfrac{dT_{cp}}{dt} = \dfrac{T_{cw}-T_{cp}}{R_{cp-cw}} - \dfrac{T_{cp}-T_{ap}}{R_{ap-cp}} - \dfrac{T_{cp}-T_{cv}}{R_{cp-cv}} & (2.4)\\
C_{aw}\dfrac{dT_{aw}}{dt} = \dfrac{T_{ew}-T_{aw}}{R_{aw-ew}} - \dfrac{T_{aw}-T_{cw}}{R_{aw-cw}} & (2.5)\\
C_{ap}\dfrac{dT_{ap}}{dt} = \dfrac{T_{ep}-T_{ap}}{R_{ap-ep}} - \dfrac{T_{ap}-T_{cp}}{R_{ap-cp}} & (2.6)\\
\dfrac{dT_{ev}}{dt} = \dfrac{\gamma-1}{\gamma}\dfrac{T_{ev}}{P_{ev}}\dfrac{dP_{ev}}{dt} & (2.7)\\
\dfrac{dT_{cv}}{dt} = \dfrac{\gamma-1}{\gamma}\dfrac{T_{cv}}{P_{cv}}\dfrac{dP_{cv}}{dt} & (2.8)\\
\dot{m}_\alpha = \dfrac{1}{\lambda_\alpha}\dfrac{T_{ep}-T_{ev}}{R_{ep-ev}} & (2.9)\\
\dot{m}_\beta = \dfrac{1}{\lambda_\beta}\dfrac{T_{cv}-T_{cp}}{R_{cp-cv}} & (2.10)
\end{cases}
$$

Mechanical equations:

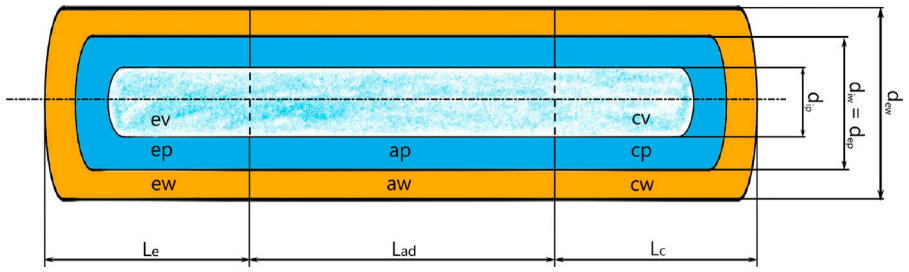

Fig. 1. Schematics of the heat pipe with notation. The control volume of vapour at the evaporator side is indicated by: **ev**; evaporator, porous control volume by: **ep**; evaporator, solid wall by: **ew**. The adiabatic, porous control volume is indicated by: **ap**; adiabatic, solid wall by: **aw**. The control volume of vapour at the condenser side is indicated by: **cv**; condenser, porous control volume by: **cp**; and the solid wall at the condenser side by: **cw**.

Table 1
List of unknowns and associated equations.

Unknown	Equation	Reference
$\dot{m}_e$	Latent heat of vaporisation definition	(2.9)
$\dot{m}_c$	Latent heat of condensation definition	(2.10)
$\dot{m}_v$	Steady-state Momentum equation for the vapour phase	(2.11)
$\dot{m}_\ell$	Steady-state Momentum equation for the liquid phase in the wick	(2.12)
P_{ev}	Steady-state Continuity and perfect gas law in the evaporator	(2.13)
$P_{cv} = P_{c\ell}$	Steady-state Continuity and perfect gas law in the condenser	(2.14)
$m_{e\ell}$	Steady-state Continuity equation in the evaporator	(2.15)
$m_{c\ell}$	Steady-state Continuity equation in the condenser	(2.16)
$P_{e\ell}$	Young–Laplace equation	(2.17)

Table 2
List of temperature unknowns and associated equations. A local thermal equilibrium assumption ensures that in the porous material (wick) the liquid and the solid phases are at the same temperature.

textbfUnknown	Equation	Reference
T_{ew}	Discretised Fourier's Equation	(2.1)
$T_{ep} = T_{e\ell}$	Discretised Fourier's Equation	(2.2)
T_{ew}	Discretised Fourier's Equation	(2.3)
$T_{cp} = T_{c\ell}$	Discretised Fourier's Equation	(2.4)
T_{aw}	Discretised Fourier's Equation	(2.5)
$T_{ap} = T_{a\ell}$	Discretised Fourier's Equation	(2.6)
T_{ev}	Time derivative of the polytropic equation	(2.7)
T_{cv}	Time derivative of the polytropic equation	(2.8)

Table 3
Geometrical characteristics of the heat pipe.

Parameter	Symbol	Value	Unit
Solid wall external radius	r_{ow}	9.55	[mm]
Solid wall internal radius	r_{iw}	9.40	[mm]
Porous wick external radius	r_{op}	9.40	[mm]
Porous wick internal radius	r_{ip}	8.65	[mm]
Evaporator axial length	L_e	600	[mm]
Adiabatic axial length	L_a	90	[mm]
Condenser axial length	L_c	200	[mm]
Effective length	L_{eff}	490	[mm]
Average pore radius	r_g	59	[μm]
Porosity	ϵ	0.9	–
Permeability	K	$1.5 \cdot 10^{-3}$	[mm^2]

$$\begin{cases} \dfrac{L_{\text{eff}}}{\pi r_{ip}^2}\dfrac{\mathrm{d}\dot{m}_v}{\mathrm{d}t} + \dfrac{8\mu_v L_{\text{eff}}}{\pi\rho_v r_{ip}^4}\dot{m}_v = -\Delta P_v - \rho_v a_z L_{\text{eff}} & (2.11)\\ \dfrac{K L_{\text{eff}}}{\mu_\ell A\epsilon}\dfrac{\mathrm{d}\dot{m}_\ell}{\mathrm{d}t} + \dfrac{L_{\text{eff}}}{\rho_\ell A}\dot{m}_\ell = -\dfrac{K}{\mu}(\Delta P_\ell + \rho_\ell a_z L_{\text{eff}}) & (2.12)\\ \dfrac{V_{ev}}{\gamma\tilde{R}T_{ev}}\dfrac{dP_{ev}}{dt} = \dot{m}_\alpha - \dot{m}_v & (2.13)\\ \dfrac{V_{cv}}{\gamma\tilde{R}T_{cv}}\dfrac{dP_{ev}}{dt} = \dot{m}_v - \dot{m}_\beta & (2.14)\\ \dfrac{dm_{e\ell}}{dt} = \dot{m}_\ell - \dot{m}_\alpha & (2.15)\\ \dfrac{dm_{c\ell}}{dt} = \dot{m}_\beta - \dot{m}_\ell & (2.16)\\ P_{ev} - P_{e\ell} = b\dfrac{2\sigma}{r_n} & (2.17) \end{cases}$$

In Eqs. (2.11) and (2.12), an effective length is introduced L_{eff}, which represents the length of the heat pipe between the condenser and the evaporator which is filled with the liquid [1].

$$L_{\text{eff}} = \frac{L_e + L_c}{2} + L_a \tag{2.18}$$

The effective thermal conductivity of the porous material, which is used in the calculation of several thermal resistances (R_{ep-ev}, R_{ap-ep}, R_{cp-cv}, R_{ap-cp}), is modelled to account for thermal conduction in such three-phase system [25] following the equation:

$$k_{\text{eff}} = \frac{k_s V_s + k_v V_v \dfrac{3k_s}{2k_s + k_v} + k_\ell V_\ell \dfrac{3k_s}{2k_s + k_\ell}}{V_s + V_v \dfrac{3k_s}{2k_s + k_v} + V_\ell \dfrac{3k_s}{2k_s + k_\ell}} \tag{2.19}$$

where v is the volume fraction.

2.2. Validation of the numerical code

The code is validated by reproducing the unsteady results by Ferrandi et al. [19]. In that work, the envelope and the porous material of the heat pipe are made of copper and the working fluid is water. The geometrical characteristics of the heat pipe are given in Table 3. All the thermophysical properties used in the simulation are displayed in Tables 4, 5 and 6. The properties of the liquid used to cool the heat pipe are instead given in Table 7. Given that not all the quantities required to perform the simulation are provided in the paper by Ferrandi et al. [19], missing quantities are extracted from saturated water tables in Incropera et al. [26] and are hypothesised not to depend on time during the simulation.

At the start of the simulation ($t = 0\,\text{s}$) the heat pipe temperature is $T_0 = 296\,\text{K}$, for $t > 0\,\text{s}$ a heat flux is imposed at the evaporator with a given time law, as displayed in Fig. 2. The thermal power provided to the system increases following a piecewise-linear law and becomes

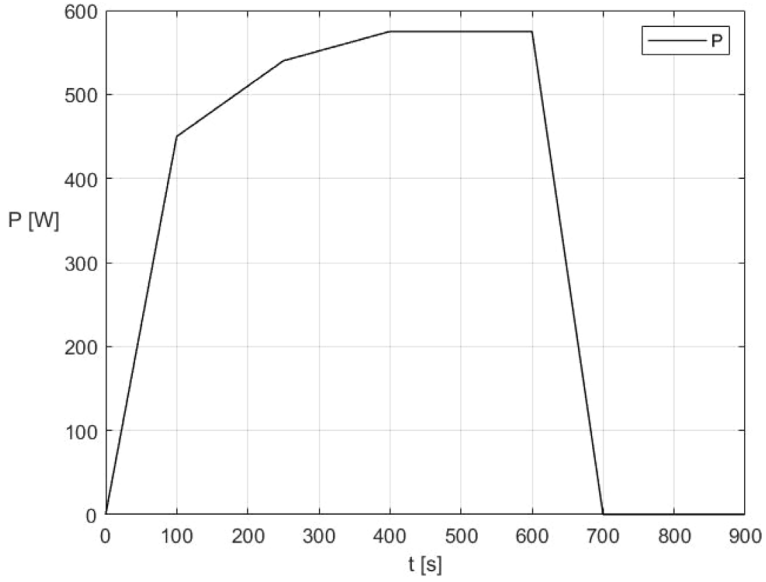

Fig. 2. Time history of the thermal power provided in input.

Table 4
Thermophysical properties of the copper.

Physical quantity	Symbol	Value	Unit
Density	ρ_s	8960	[kg/m^3]
Thermal conductivity	k_s	390	[W/mK]
Specific heat	c_s	385	[J/kgK]

Table 5
Thermophysical properties of the saturated liquid water.

Physical quantity	Symbol	Value	Unit
Density	ρ_ℓ	979	[kg/m^3]
Thermal conductivity	k_ℓ	0.660	[W/mK]
Specific Heat	c_ℓ	4188	[J/kgK]
Viscosity	μ_ℓ	$420 \cdot 10^{-6}$	[Pa s]
Surface Tension	σ_ℓ	0.065	[N/m]
Latent Heat of Vaporisation	λ_l	2342	[kJ/kg]

Table 6
Thermophysical properties of the saturated vapour.

Physical quantity	Symbol	Value	Unit
Density	ρ_v	0.17	[kg/m^3]
Specific Heat	c_v	1930	[J/kgK]
Viscosity	μ_v	$10.69 \cdot 10^{-6}$	[$Pa\ s$]
Specific heat ratio	γ_v	1.31	[−]
Perfect gas constant	R_v	461.50	[J/kgK]

Table 7
Thermophysical properties of the cooling water at 296.2 K.

Quantity	Symbol	Value	Unit
Density	ρ_f	998	[kg/m^3]
Specific Heat	c_f	4181	[J/kgK]

constant after 400 s. At time level $t = 600$ s, the thermal power starts to decrease with a linear time law until the time level $t = 700$ s where it is turned off (0 W) and kept at 0 W until the end of the simulation, at $t = 900$ s.

The time histories of temperature at the evaporator wall, condenser wall and of vapour are displayed in Fig. 3. During the transient (from $t = 0$ to $t = 430$) results are extracted at three different time levels:

- $t_1 = 66$ s
- $t_2 = 130$ s
- $t_3 = 225$ s

Table 8
Comparison between present results and results extracted from figures in the literature. Comparisons are performed after a time of $t = 66$ s from the start of the experiment or simulation.

	Present	Ref. [19]	Ref. [5]	Ref. [15]	Err. % WRT [19]
T_{pe} (K)	315.99	315.72	315.50	316.00	0.09
T_{ve} (K)	313.59	313.20	313.00	313.00	0.12
T_{pc} (K)	306.96	306.34	304.00	305.50	0.20

Table 9
Comparison between present results and results extracted from figures in the literature. Comparisons are performed after a time of $t = 130$ s from the start of the experiment or simulation.

	Present	Ref. [19]	Ref. [5]	Ref. [15]	Err. % WRT [19]
T_{pe} (K)	332.49	331.43	331.00	330.00	0.32
T_{ve} (K)	328.41	327.46	328.00	326.00	0.29
T_{pc} (K)	316.29	315.62	312.50	313.00	0.21

one additional result is extracted in the steady state, (see Fig. 3). In the Figure, temperatures considered for comparisons are indicated by circles. Comparison is shown in Tables 8, 9 and 10. The results obtained by the present implementation are compared against the results published by Ferrandi [19], experimental results published by Huang et al. [5] and numerical results provided by Tournier & El Genk [15]. Numbers reported in the Tables for the numerical and experimental results are extracted graphically from the pictures in the literature. The comparison in steady conditions reached at the time instant $t = 430$ s, is provided in Table 11. The last column of the tables shows the percentage error in temperature with reference to the results published by Ferrandi et al. [19]. It should be clear to the reader that introducing a percentage error on temperature, which is defined apart from a constant, provides errors depending on the scale used for temperature. The Kelvin scale of temperatures is selected in this case.

Results in steady state are again compared against [19], [5] and [15], and against the analytical results by Zhu & Vafai [13]. The comparison is shown in Table 11.

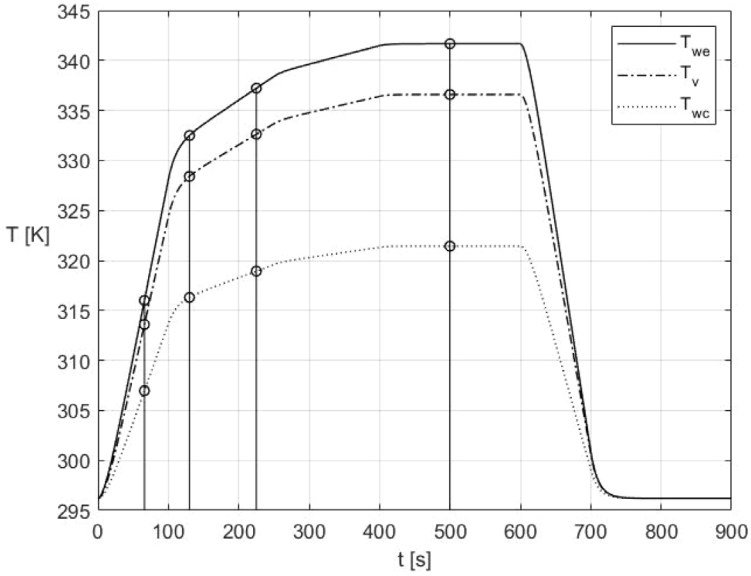

Fig. 3. Time history of the space-averaged temperature at the evaporator wall, condenser wall and in the vapour phase, together with the indication of time instants selected for validation.

Table 10
Comparison between present results and results extracted from figures in the literature. Comparisons are performed after a time of $t = 225$ seconds from the start of the experiment or simulation.

	Present	Ref. [19]	Ref. [5]	Ref. [15]	Err. % WRT [19]
T_{pe} (K)	337.22	337.68	338.00	338.00	0.14
T_{ve} (K)	332.62	333.11	335.00	333.00	0.15
T_{pc} (K)	318.93	319.28	319.00	318.00	0.11

Table 11
Comparison between present results and results extracted from figures in the literature. Comparisons are carried out when the steady state is reached.

	Present	Ref. [19]	Ref. [5]	Ref. [15]	Ref. [13]	Err. % WRT [19]
T_{pe}	341.67	341.59	341.50	342.00	341.00	0.52
T_{ve}	336.60	336.62	338.50	337.50	337.00	0.50
T_{pc}	321.43	321.55	322.00	321.00	321.50	0.49

3. Applications and results

3.1. Effects of accelerations on heat pipe performance

When a heat pipe is used as the cooling system for a power module mounted on a vehicle, it is subject to unsteady thermal power input and time-varying accelerations which can alter its thermal behaviour of a non-negligible amount. To investigate the possibility of using a heat pipe as a cooling system for a high-performance car, two simulations are carried out. Both make use of the same boundary and initial conditions and the same time history of the thermal power in input. The difference between the simulations is that while one accounts for the effect of acceleration, the other is carried out in an inertial system of reference. The heat pipe under scrutiny is mounted on the power module so that its axis is orthogonal to the longitudinal axis of the car and parallel to the ground. In this configuration, accelerations due to curvilinear trajectories are maximum and parallel to the heat pipe axis. In the configuration investigated, the condenser is towards the right part of the car. The heat pipe chosen for cooling the power module is a water–copper heat pipe whose geometry is detailed in Table 12. The heat pipe is cooled with water at the condenser wall.

Data used for tests are taken from the time history of electric power dissipated by a chip mounted on a high-performance car and the car's accelerations during cornering. These have been collected during a test session at the Austrian Spielberg circuit, shown in Fig. 4 and thus are fully real. The segment represented in the simulation is delimited by point A and B in Fig. 4.

Table 12
Geometrical characteristics of the heat pipe.

Parameter	Symbol	Value	Unit
Radii			
Solid wall, external	r_{ow}	10	[mm]
Solid wall, internal	r_{iw}	9.8	[mm]
Porous wick, external	r_{op}	9.8	[mm]
Porous wick, internal	r_{ip}	9.4	[mm]
Axial lengths			
Evaporator	L_e	15	[mm]
Adiabatic	L_a	8	[mm]
Condenser	L_c	40	[mm]

At the start of the simulation, the system at the temperature of $T_0 = 333.15$ K, the same temperature as the cooling water at the condenser wall. Initial conditions are prepared by keeping the heat generated by the chip for a short time interval (10 s) at the same value as the first record of the experimental campaign. A pre-heating is thus used to start the simulation. After 38 s the heat transferred by the heat pipe is set to zero.

The time evolution of temperature levels of the evaporator wall and the condenser wall are shown in Fig. 5. The curve in Fig. 5 is for an accelerated frame of reference. Differences between calculations carried out in an accelerated frame of reference and inertial frame are shown in Fig. 6. Results obtained suggest that the contribution of the centripetal acceleration in the case of cornering is, although small, non-negligible and it should be accounted for when the design is carried out very close to limit conditions.

The dependence of results on the time step of the lumped parameter procedure Δt_{TN} is investigated. Two tests are carried out, the first uses a time step fifty times the one employed in the simulation presented in the paper ($\Delta t_{TN} = 5\times10^{-5}$ s instead of $\Delta t_{TN} = 1\times10^{-6}$ s). The procedure in this case undergoes numerical instability and convergence is not attained. A second test has been carried out using a time step of 5×10^{-7} s. This corresponds to a temporal discretisation which is twice as fine as the simulation reported in the manuscript. The difference between the two solutions is deemed negligible: the temperature at the condenser in the second peak ($t = 17.3$ s) differs only by $\Delta T = 0.0031$ degrees. For

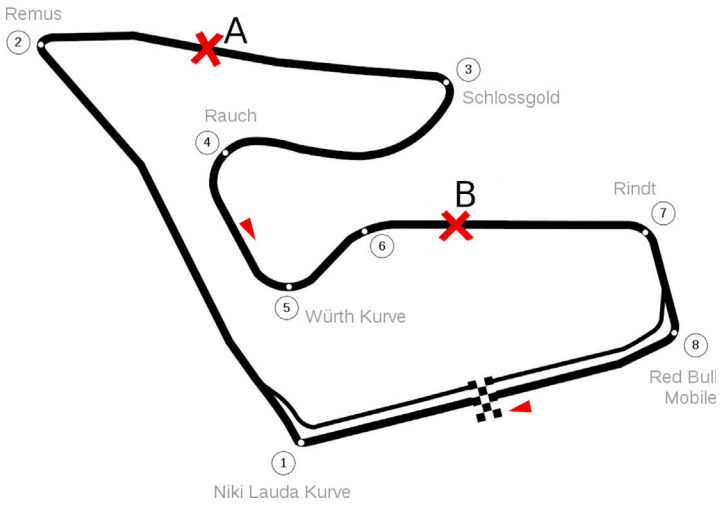

Fig. 4. Spielberg circuit, (A) Start of the simulation, (B) End of the simulation.

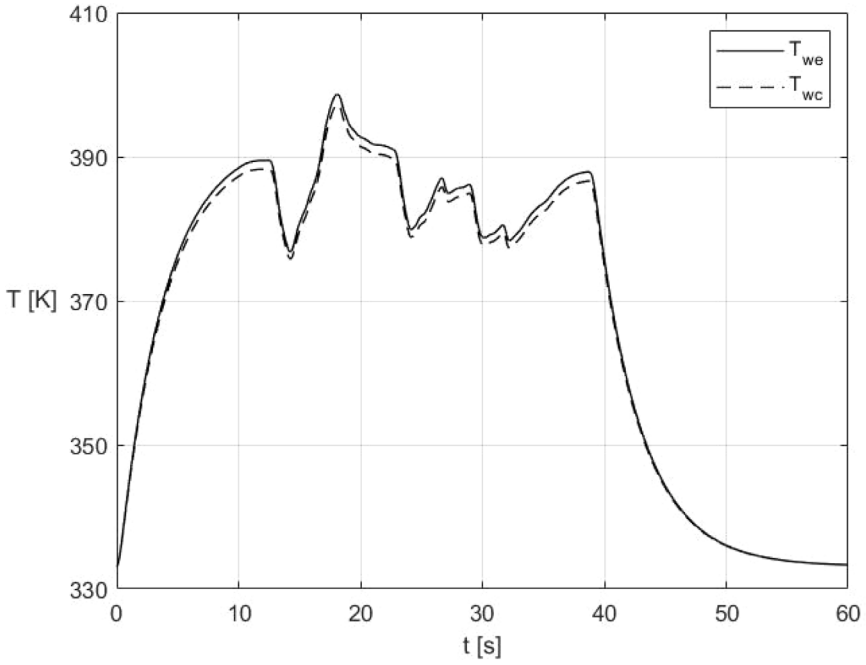

Fig. 5. Time history of the temperatures of the heat pipe in an accelerated environment.

the case discussed here, a time step small enough to prevent numerical instability can represent all the physical time scales of the unsteady problem.

3.2. Results from the 1D/3D co-simulation

A 1D/3D co-simulation is used here to study the thermodynamic behaviour of a power module mounted onboard a high-performance car. The aim is here to check that the chip and the solid region in contact with the chip stay under the maximum allowable temperature, $T_{max} = 440$ K.

In the context of this work, where the 3D approach is used to represent conduction in the heat-generating chip and in the solid component which connects the chip to the heat pipe (see Fig. 8 for a symmetric slice of the component), the 1D/3D co-simulation method does not contribute with a noticeable accuracy improvement of the numerical model because the heat transfer problem does not include convection which is the most difficult phenomenon to represent accurately in a thermal network. Accordingly, the 1D/3D co-simulation described here should be regarded as a proof-of-concept.

A portion of the power module composed of only one chip is considered together with the layers of different materials between the chip and the heat pipe, as shown in Fig. 7(a). All the boundaries of the domain are set as adiabatic except for the interface, which is at a fixed temperature, between the heat pipe and the conducting layers, see Fig. 8 and Table 13. Both geometry and boundary conditions are symmetric with respect to two orthogonal axes, so only one-fourth of the domain is modelled. Given the simplicity of the geometry, a grid made of hexahedral elements is used to discretise the domain, as shown in Fig. 7(c). The three-dimensional chip is modelled as a

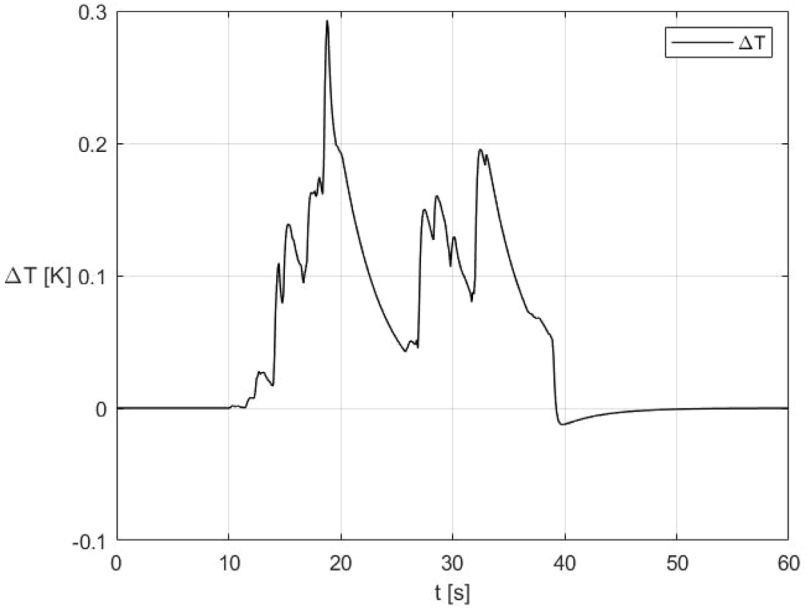

Fig. 6. Time history of the difference between the wall temperature at the evaporator in the accelerated environment and in the absence of lateral accelerations.

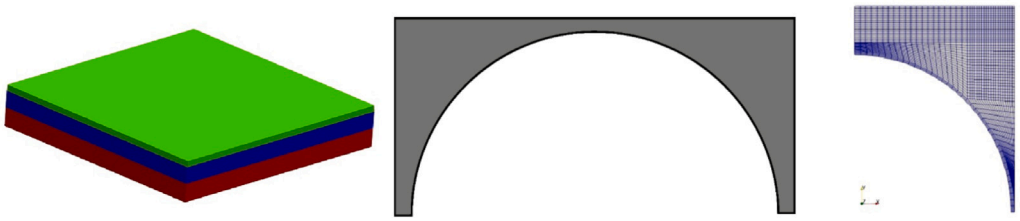

Fig. 7. (a) Layout of the power module's portion considered: the green portion represents the chip, the blue portion represents the copper layer, and the red portion represents a layer of ceramic material. (b) Geometry of the aluminium element enclosing the heat pipe. (c) Mesh used to simulate the power module. (For interpretation of the references to colour in this figure legend, the reader is referred to the web version of this article.)

Table 13
List of boundary conditions applied. The acronym AEI stands for Aluminium–Evaporator Interface.

Boundary	Boundary condition
Left	Symmetry Plane
Back	Symmetry Plane
Top	Adiabatic
Front	Adiabatic
Right	Adiabatic
Bottom	Adiabatic
AEI	Fixed Temperature

uniform, volumetric source of thermal power, while the copper layer, the ceramic layer and the curved aluminium element enclosing the heat pipe do not generate heat, see Fig. 7(b).

In this 1D/3D co-simulation approach, a procedure in which alternately updates solutions in the 1D and 3D domains is required. This procedure is repeated to advance in time the solution. The algorithm works as follows:

1. Start the 3D simulation at time level 0 by setting the temperature field to a uniform value $T^{(n=0)}$ (ICs). The initial temperature field meets the boundary conditions enforced, see Table 13.
2. Solve the three-dimensional conduction equation in the solid, accounting for the heat generated in the chip $\dot{Q}^{(n-1)}$, which is a function of time. This allows for the calculation of the temperature field at time level n, $T^{(n)}$. The thermal power exchanged

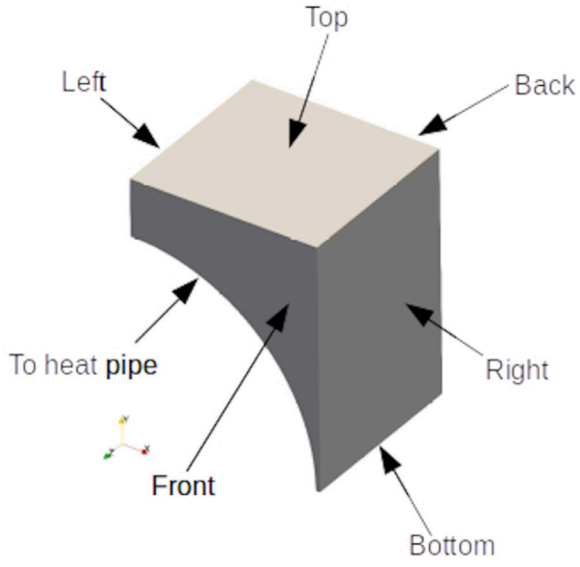

Fig. 8. Boundary conditions enforced on the computational domain.

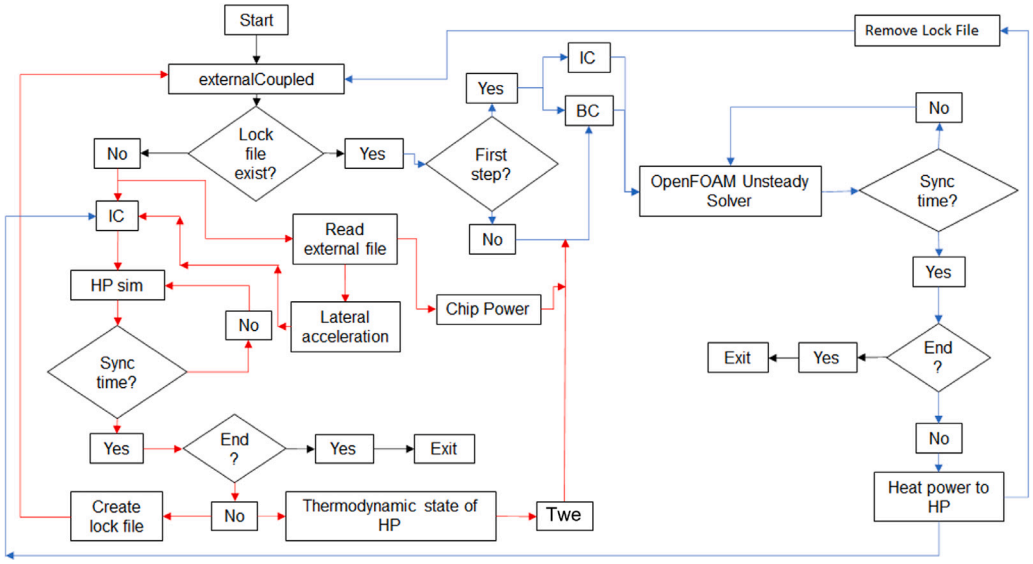

Fig. 9. Flow diagram of the 1D/3D co-simulation.

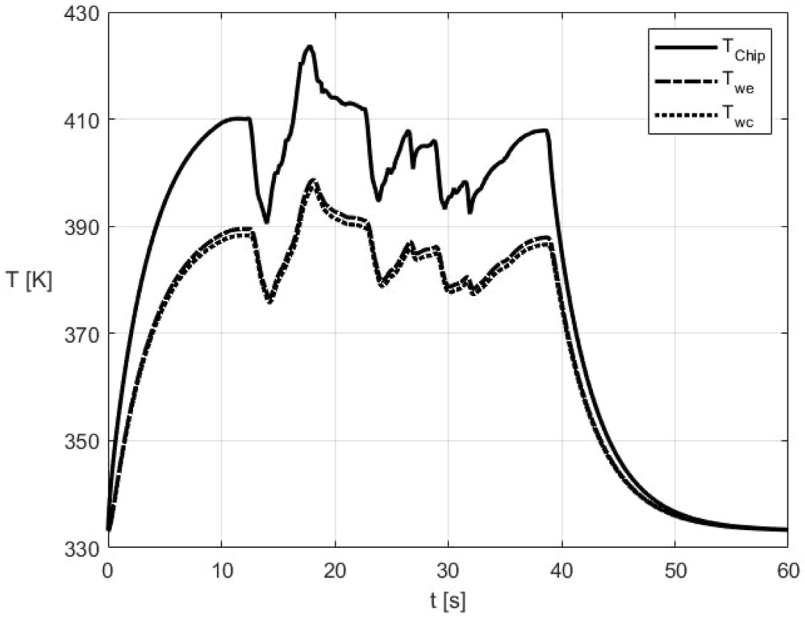

Fig. 10. Time history of the heat pipe temperatures at the evaporator wall, the condenser wall and the spatially averaged temperature of the chip in an accelerated environment.

with the heat pipe is calculated from the temperature gradient at the interface between the aluminium element and evaporator AEI (Aluminium–Evaporator Interface).

3. Solve the thermal network representing the heat pipe. This provides the temperature at the AEI.
4. Update the temperature BCs at AEI in the 3D code.
5. For each time step repeat the process from point 2 to 4 to get $T^{(n+1)}$ from T^n up to the final time of the physical process to be represented.

The flow diagram of the 1D/3D co-simulation is shown in Fig. 9.

Given the time-advancement scheme of the 3D model is very different from the time treatment in the LPTN which represents the heat pipe, the time steps required by the two methods can greatly differ. In the present case, the time step employed in the LPTN, $\Delta t_{\mathrm{TN}} = 1\,e^{-6}$ s is four orders of magnitude smaller than the time step required by the 3D solver *OpenFOAM* $\Delta t_{\mathrm{OF}} = 1\,e^{-2}$ s. Therefore subcycling is applied and in order to pass from step 2 to 4 of the above pseudocode, multiple LPTN steps are performed.

The output of the 1D/3D co-simulation is composed of:

- the time history of all the unknowns listed in Tables 1 and 2;
- the temperature distribution on the chip, copper layer, ceramic layer and aluminium element at each time.

The time history of the temperature at the evaporator wall, at the wall of the condenser and the volume-averaged temperature of the chip, are displayed in Fig. 10.

Fig. 10 shows that the chip reaches its maximum volume-averaged temperature at $t = 17.3$ s. Given the value is pretty close to the maximum allowed temperature, a check is done to ensure that $T_{\max} = 440$ K is never reached, also locally. Fig. 11 shows temperature distributions in the power module at the time level under scrutiny ($t = 17.3$ s). It is finally checked directly from the figures, that the maximum temperature reached by the chip remains below the threshold value.

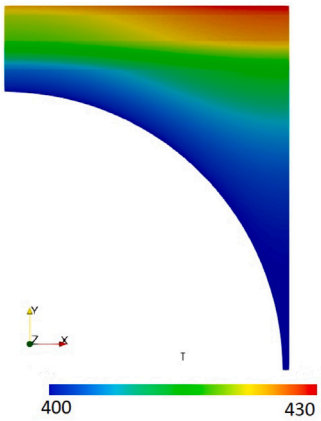

(a) Front view

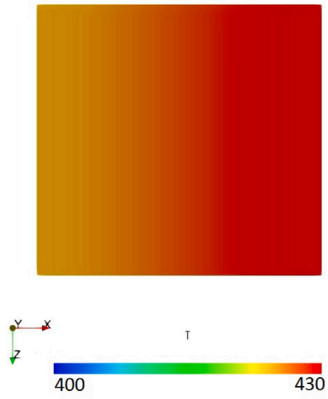

(b) Top view: chip

Fig. 11. Temperature distribution inside the power module, at time $t = 17.3$ s, corresponding to the most critical situation.

The temperature difference between the case where centripetal acceleration is accounted for and the one where the acceleration is neglected is about $\Delta T = 0.3$ K. The maximum acceleration of the system is order $3g$, over a time interval of 0.01 s. This amounts to an impulse about 0.3 Ns.

Coupling a lumped parameter approach to a 3D simulation is a convenient method to investigate detailed temperature distributions of the most critical regions in systems where the operating temperature interval is under control. This approach is computationally inexpensive and fast. It can also be very accurate, moreover, it naturally includes multi-physics.

4. Conclusions

In this paper, we investigate the possibility of using a heat pipe for the thermal management of power modules, for application in high-performance cars. The thermodynamic behaviour of the heat pipe is represented through an LPTN approach implemented in Python. The code is validated against numerical results and experimental results. For the steady-state, it is also compared to the analytical solution. Validation results ensure that the code is accurate and can be conveniently used to simulate the thermal behaviour of heat pipes in road vehicle applications.

The LPTN code is coupled to a $3D$ code to implement a 1D/3D co-simulation. This is used to study the thermal behaviour of the power module. The approach presented in this paper allows us to calculate the spatial distribution of the temperature in selected critical portions of the system, at low computational cost.

In the example application presented, the temperature difference between the case where centripetal acceleration is accounted for and the one where the acceleration is neglected is about $\Delta T = 0.3$ K. The maximum acceleration of the system is order $3g$, over a time interval of 0.01 s. This amounts to an impulse of about 0.3 Ns. This suggests that, for the heat pipes considered here, the effect of fictitious forces cannot be neglected in cases where the maximum impulse $\int a\,\mathrm{d}t$ is order 0.3 Ns or larger and the target accuracy on temperature levels is small.

Nomenclature

- A - Cross section area
- a - Acceleration
- b - Correction Coefficient (see [19])
- C - Heat capacity
- c - Specific heat
- d - Derivative symbol
- K - Permeability
- k - Thermal conductivity
- L - Axial length
- m - Mass
- $\dot{m}$ - Mass flow rate
- P - Pressure
- $\dot{Q}$ - Thermal power
- R - Thermal resistance
- $\tilde{R}$ - Gas constant
- r - Radius
- T - Temperature
- t - Time
- V - Volume
- $\mathbf{v}$ - Velocity vector
- w - Axial velocity
- z - Axial direction

Subscripts

- TN - Thermal network
- OF - OpenFOAM
- a - Adiabatic section
- c - Condenser
- e - Evaporator

- eff - Effective
- f - Fluid
- g - Grain
- i - Inner
- in - Entering
- ℓ - Liquid
- n - Capillary
- o - Outer
- p - Porous material (wick)
- s - Solid
- v - Vapour
- w - Solid wall

Greek symbols

- α - Evaporated
- β - Condensed
- γ - Specific heat ratio
- ϵ - Porosity
- λ - Latent heat of vaporisation
- μ - Dynamic viscosity
- ρ - Density
- σ - Surface tension

CRediT authorship contribution statement

Matteo Ermini: Validation, Software, Resources, Methodology, Formal analysis. **Massimo Sabato:** Supervision. **Federico Brusiani:** Supervision, Data curation. **Thierry Baritaud:** Supervision. **Roberto Corsini:** Supervision. **Enrico Stalio:** Supervision, Methodology, Conceptualization.

Declaration of competing interest

The authors declare that they have no known competing financial interests or personal relationships that could have appeared to influence the work reported in this paper.

Data availability

The data that has been used is confidential.

Appendix A. Demonstration of the momentum equation form employed in the vapour duct

The momentum equation in laminar, fully developed conditions projected along the z direction for constant properties and $r \neq 0$ is

$$\rho \frac{\partial w}{\partial t} = -\frac{\mathrm{d}p}{\mathrm{d}z} + \mu \frac{1}{r}\frac{\partial}{\partial r}\left(r\frac{\partial w}{\partial r}\right) - \rho a_z \tag{A.1}$$

where in the laminar flow hypothesis $w_\theta = w_r = 0$ is included. In Eq. (A.1) the last term is due to a non-inertial frame of reference of acceleration $\mathbf{a} = (a_r, a_\theta, a_z)$. By multiplying by r ($r \neq 0$):

$$\rho r \frac{\partial w}{\partial t} = -r\frac{\mathrm{d}p}{\mathrm{d}z} + \mu \frac{\partial}{\partial r}\left(r\frac{\partial w}{\partial r}\right) - \rho a_z r \tag{A.2}$$

By integration between $r = 0$ and the generic r

$$\rho \frac{r^2}{2}\frac{\partial w}{\partial t} = -\frac{r^2}{2}\frac{\mathrm{d}p}{\mathrm{d}z} + \mu r \frac{\partial w}{\partial r} - \rho a_z \frac{r^2}{2} \tag{A.3}$$

Division by r ($r \neq 0$) and integration between r and the wall (r_{ip}) results in:

$$\rho_v \frac{r_{ip}^2 - r^2}{4}\frac{\partial w}{\partial t} = -\frac{r_{ip}^2 - r^2}{4}\frac{\mathrm{d}p}{\mathrm{d}z} + \mu w - \rho_v a_z \frac{r_{ip}^2 - r^2}{4} \tag{A.4}$$

Now, introducing the definition of mass flow rate:

$$\dot{m} = \int_0^{r_{ip}} 2\pi\ \rho_v w\, r dr \tag{A.5}$$

and by integrating between $r = 0$ and $r = r_{ip}$, under the hypothesis that $\frac{\partial w}{\partial t}$ does not depend upon r the Poiseuille equation in an accelerated reference frame becomes:

$$\frac{1}{\pi r_{ip}^2}\frac{\partial \dot{m}}{\partial t} + \frac{8\mu}{\pi \rho_v r_{ip}^4}\dot{m} = -\frac{\mathrm{d}p_v}{\mathrm{d}z} - \rho_v a_z \tag{A.6}$$

Eventually, by integrating along the axial direction z between $z = 0$ and $z = L_{\mathrm{eff}}$, the equation becomes:

$$\frac{L_{\mathrm{eff}}}{\pi r_{ip}^2}\frac{\mathrm{d}\dot{m}}{\mathrm{d}t} + \frac{8\mu L_{\mathrm{eff}}}{\pi \rho r_{ip}^4}\dot{m} = \left(P_v(0) - P_v(L_{\mathrm{eff}})\right) - \rho_v a_z L_{\mathrm{eff}} \tag{A.7}$$

which corresponds to (2.11).

Appendix B. Demonstration of the momentum equation form employed in the porous medium

The momentum equation employed for the porous medium can be derived following the work by Whitaker [27,28]. Whitaker applies the volume averaging technique to the Navier–Stokes equations in order to obtain the Darcy's law with the Forchheimer correction for homogeneous porous media. Volume averaging is capable of representing the very complex physical reality, clearly described in detailed numerical simulations [29,30], through a set of differential equations, not too unlike those valid in the clear fluid. As reported in Ref. [28], two different volume averages can be defined. The superficial phase average:

$$\langle \psi \rangle = \frac{1}{V}\int_{V_\ell} \psi dV \tag{B.1}$$

and the intrinsic phase average, defined as:

$$\langle \psi \rangle^\ell = \frac{1}{V_\ell}\int_{V_\ell} \psi dV \tag{B.2}$$

These two are related by:

$$\langle \psi \rangle = \epsilon \langle \psi \rangle^\ell \tag{B.3}$$

Where V_ℓ is the volume of the fluid phase while V includes both the solid and the fluid. By applying the volume averaging technique, the Navier–Stokes equations become:

$$\begin{aligned}\rho\frac{\partial \langle \mathbf{v}\rangle^\ell}{\partial t} + \rho\langle \mathbf{v}\rangle^\ell \nabla\cdot\langle \mathbf{v}\rangle^\ell + \underbrace{\rho\epsilon^{-1}\nabla\cdot\langle \tilde{\mathbf{v}}\otimes\tilde{\mathbf{v}}\rangle}_{\text{Volume Filter}} \\ = -\nabla\langle P\rangle^\ell + \underbrace{\mu\nabla^2\langle \mathbf{v}\rangle^\ell}_{\substack{\text{Brinkman}\\ \text{correction}}} + \rho(\mathbf{g}-\mathbf{a}) + \underbrace{\frac{1}{V_\ell}\int_{A_{\sigma\ell}} n_{\ell\sigma}(-\tilde{P}\mathbf{I} + \mu\nabla\tilde{\mathbf{v}})dA}_{\text{Surface Filter}}\end{aligned} \tag{B.4}$$

where the tilde indicates a spatial deviation, defined as:

$$\psi = \langle \psi \rangle^\ell + \tilde{\psi} \tag{B.5}$$

For isotropic, homogeneous porous media the 3rd term on the left-hand side and the Brinkman correction term, vanish. The second term on the left-hand side vanishes upon the hypothesis of constant density, together with $\rho\mathbf{g}$ which is uniform in space. Finally, the equation reduces to:

$$\rho\frac{\partial \langle \mathbf{v}\rangle^\ell}{\partial t} = -\nabla\langle P\rangle^\ell - \rho\mathbf{a} + \frac{1}{V}\int_{A_{\sigma\ell}} n_{\ell\sigma}(-\tilde{P}\mathbf{I} + \mu\nabla\tilde{u})dA \tag{B.6}$$

the surface filter is modelled by the Forchheimer approximation:

$$\frac{1}{V_\ell}\int_{A_{\sigma\ell}} n_{\ell\sigma}(-\tilde{P}\mathbf{I} + \mu\nabla\tilde{\mathbf{v}})dA = -\frac{\mu}{K}(\mathbf{I}+\mathbf{F})\cdot\langle \mathbf{v}\rangle \tag{B.7}$$

where $\mathbf{F}$ is the tensor of the Forchheimer correction. For small Re the term including $\mathbf{F}$ can be neglected and:

$$\rho\frac{\partial \langle \mathbf{v}\rangle^\ell}{\partial t} = -\nabla\langle P\rangle^\ell - \rho\mathbf{a} - \frac{\mu_\ell}{K}\langle \mathbf{v}\rangle \tag{B.8}$$

Using the superficial velocity in all the terms and projecting the equation along z, in the hypothesis that all quantities do not vary in the directions orthogonal to z, results in:

$$\frac{K}{\nu_\ell \epsilon}\frac{\partial \langle w\rangle}{\partial t} + \langle w\rangle = -\frac{K}{\mu_\ell}\left(\frac{\mathrm{d}}{\mathrm{d}z}\langle P\rangle^\ell + \rho a_z\right) \tag{B.9}$$

Integrating in the axial (z) direction between $z = 0$ and $z = L_{\text{eff}}$ and by defining ΔP as the difference in $\langle P\rangle^\ell$ between 0 and L_{eff}:

$$\frac{K L_{\text{eff}}}{\nu_\ell \epsilon}\frac{\partial \langle w\rangle}{\partial t} + \langle w\rangle L_{\text{eff}} = -\frac{K}{\mu_\ell}(\Delta P + \rho a_z L_{\text{eff}}) \tag{B.10}$$

The mass flow rate is given by:

$$\dot{m}_\ell = \rho_\ell A \langle w\rangle \tag{B.11}$$

where A includes both the fluid and the solid regions. Substitution in Eq. (B.10) gives:

$$\frac{K L_{\text{eff}}}{\mu_\ell A \epsilon}\frac{\mathrm{d}\dot{m}_\ell}{\mathrm{d}t} + \frac{L_{\text{eff}}}{\rho_\ell A}\dot{m}_\ell = -\frac{K}{\mu_\ell}(\Delta P + \rho_\ell a_z L_{\text{eff}}) \tag{B.12}$$

which corresponds to (2.12).

References

[1] D. Reay, P. Kew, R. McGlen, Heat Pipes (Sixth Edition), Sixth ed., Butterworth-Heinemann, Oxford, 2014, pp. 175–206, http://dx.doi.org/10.1016/B978-0-08-098266-3.00007-8.

[2] R.J. McGlen, R. Jachuck, S. Lin, Integrated thermal management techniques for high power electronic devices, Appl. Therm. Eng. 24 (8) (2004) 1143–1156, http://dx.doi.org/10.1016/j.applthermaleng.2003.12.029.

[3] C. Zaghdoudi, C. Tantolin, C. Sarno, Experimental investigation on the use of flat mini heat pipes for avionics electronic modules cooling, Int. Rev. Mech. Eng. 5 (2011) 770–883.

[4] K.-S. Kim, M.-H. Won, J.-W. Kim, B.-J. Back, Heat pipe cooling technology for desktop PC CPU, Appl. Therm. Eng. 23 (9) (2003) 1137–1144, http://dx.doi.org/10.1016/S1359-4311(03)00044-9.

[5] L. Huang, M. El-Genk, J.-M. Tournier, Transient performance of an inclined water heat pipe with a screen wick, 236, 1993, pp. 87–92.

[6] M.S. El-Genk, H. Lianmin, An experimental investigation of the transient response of a water heat pipe, Int. J. Heat Mass Transfer 36 (15) (1993) 3823–3830, http://dx.doi.org/10.1016/0017-9310(93)90062-B.

[7] B.D. Iverson, S.V. Garimella, Experimental measurements of heat and mass transport in heat pipe wicks, in: Proceedings of the ASME Heat Transfer/Fluids Engineering Summer Conference 2004, HT/FED 2004, vol. 1, 2004, pp. 209–217.

[8] R.-T. Wang, J.-C. Wang, Analyzing the pressure-difference phenomenon between the condensing and boiling sections in a heat pipe cooling system, Int. Commun. Heat Mass Transfer 39 (3) (2012) 390–398.

[9] S.K. Thomas, K.L. Yerkes, Quasi-steady-state performance of a heat pipe subjected to transient acceleration loadings, J. Thermophys. Heat Transfer 11 (2) (1997) 306–309, http://dx.doi.org/10.2514/2.6239.

[10] V. Kiseev, A. Belonogov, A. Belyaev, Influence of adverse accelerations on the operation of an "Antigravity" heat pipe, J. Eng. Phys. 50 (1986) 394–398, http://dx.doi.org/10.1007/BF00871059.

[11] M.C. Zaghdoudi, C. Sarno, Investigation on the effects of body force environment on flat heat pipes, J. Thermophys. Heat Transfer 15 (4) (2001) 384–394, http://dx.doi.org/10.2514/2.6640.

[12] S. Riffat, X. Zhao, P. Doherty, Analytical and numerical simulation of the thermal performance of 'mini' gravitational and 'micro' gravitational heat pipes, Appl. Therm. Eng. 22 (9) (2002) 1047–1068, http://dx.doi.org/10.1016/S1359-4311(02)00029-7.

[13] N. Zhu, K. Vafai, Analysis of cylindrical heat pipes incorporating the effects of liquid–vapor coupling and non-darcian transport — A closed form solution, Int. J. Heat Mass Transfer 42 (18) (1999) 3405–3418, http://dx.doi.org/10.1016/S0017-9310(99)00017-4.

[14] M. Piller, S. Polidoro, E. Stalio, Multiplicity of solutions for laminar, fully-developed natural convection in inclined, parallel-plate channels, Int. J. Heat Mass Transfer 79 (2014) 1014–1026, http://dx.doi.org/10.1016/j.ijheatmasstransfer.2014.08.072.

[15] J.. Tournier, M.S. El-Genk, A heat pipe transient analysis model, Int. J. Heat Mass Transfer 37 (5) (1994) 753–762.

[16] H. Sun, S. Tang, C. Wang, J. Zhang, D. Zhang, W. Tian, S. Qiu, G. Su, Numerical simulation of a small high-temperature heat pipe cooled reactor with CFD methodology, Nucl. Eng. Des. 370 (2020).

[17] T. Höhne, CFD simulation of a heat pipe using the homogeneous model, Int. J. Thermofluids 15 (2022) 100163, http://dx.doi.org/10.1016/j.ijft.2022.100163.

[18] Z.J. Zuo, A. Faghri, A network thermodynamic analysis of the heat pipe, Int. J. Heat Mass Transfer 41 (11) (1998) 1473–1484.

[19] C. Ferrandi, F. Iorizzo, M. Mameli, S. Zinna, M. Marengo, Lumped parameter model of sintered heat pipe: Transient numerical analysis and validation, Appl. Therm. Eng. 50 (1) (2013) 1280–1290, http://dx.doi.org/10.1016/j.applthermaleng.2012.07.022.

[20] R. Caruana, L. Gallazzi, R. Iazurlo, M. Marcovati, M. Guilizzoni, A multi-node lumped parameter model including gravity and real gas effects for steady and transient analysis of heat pipes, Fluids 7 (3) (2022) http://dx.doi.org/10.3390/fluids7030109.

[21] O. Koekemoer, C. du Toit, P. Niemand, Investigation into different 1D/3D co-simulation methodologies applied to a natural circulation loop, Nucl. Eng. Des. 390 (2022) 111698, http://dx.doi.org/10.1016/j.nucengdes.2022.111698, URL https://www.sciencedirect.com/science/article/pii/S0029549322000528.

[22] P. Lu, Q. Gao, Y. Wang, The simulation methods based on 1D/3D collaborative computing for the vehicle integrated thermal management, Appl. Therm. Eng. 104 (2016) 42–53.

[23] N. Watanabe, M. Kubo, N. Yomoda, An 1D-3D integrating numerical simulation for engine cooling problem, SAE Technical Papers (2006).

[24] J. Sun, K. Nawaz, J. Rendall, A. Elatar, J. Brechtl, Heat pump water heater enhanced with phase change materials thermal energy storage: Modeling study, Int. Commun. Heat Mass Transfer 146 (2023).

[25] D. Chaudhary, R. Bhandari, Heat transfer through a three-phase porous medium, J. Phys. D: Appl. Phys. 1 (6) (1968) 815.

[26] F. Incropera, D. DeWitt, T. Bergman, A. Lavine, Fundamentals of Heat and Mass Transfer, Wiley, 2007.

[27] S. Whitaker, The forchheimer equation: A theoretical development, Transp. Porous Media 25 (1) (1996) 27–61.

[28] S. Whitaker, Flow in porous media I: A theoretical derivation of Darcy's law, Transp. Porous Media 1 (1986) 3–25, http://dx.doi.org/10.1007/BF01036523.

[29] M. Piller, A. Boschetto, E. Stalio, G. Schena, O. Errico, Pore-scale simulation of laminar flow through a sample of aluminum foam, J. Porous Media 16 (9) (2013) 777–793, http://dx.doi.org/10.1615/JPorMedia.v16.i9.10.

[30] J. Qin, Z. Xu, Z. Liu, F. Lu, C. Zhao, Pore-scale investigation on flow boiling heat transfer mechanisms in open-cell metal foam by LBM, Int. Commun. Heat Mass Transfer 110 (2020).